Materials Transactions, Vol. 65, No. 12 (2024) pp. 1464 to 1472

Numerical Analysis to Evaluate the Effect of Cooling Rates on Microstructures in Casted Cu-Ni-Si Alloys by Phase-Field Simulation

Yuki Muto[1,*1,*2], Kazuki Kammuri[1], Junji Miyake[2], Machiko Ode[3], Tetsusei Kurashiki[4] and Hiroaki Mori[4]

[1]*Kurami Branch, Technology Development Center, JX Advanced Metals Corporation, Koza-gun, Kanagawa 253-0101, Japan*
[2]*First Division, JX Advanced Metals Research Institute for Technology & Strategy Co., Ltd., Tokyo 105-0001, Japan*
[3]*Structural Thermodynamics Group, Research Center for Structural Materials, National Institute for Materials Science (NIMS), Tsukuba 305-0047, Japan*
[4]*Graduate School of Engineering, Osaka University, Suita 565-0871, Japan*

Corson (Cu-Ni-Si) alloys were unidirectionally solidified via the Mizuta method under air or water cooling. To replicate the microstructure of a Corson alloy during solidification, phase-field (PF) simulations were performed, and the numerical results were compared with the experimental findings. The comparison between the air- and water-cooling conditions revealed that the primary dendrite trunks were thinner, and the secondary dendrites were longer and more developed under air-cooling conditions. These results were consistent with the experimental observations. Furthermore, the secondary dendrite arm spacings were evaluated via PF simulations, and the calculated results were consistent with the experimental observations. The interface energy and its anisotropy adopted in the present PF simulations were reasonable for the Corson alloy when compared with the values reported in other studies. [doi:10.2320/matertrans.MT-M2024098]

(Received July 4, 2024; Accepted September 15, 2024; Published November 25, 2024)

Keywords: *Corson alloy, unidirectional solidification, microstructure, phase-field, secondary dendrite arm spacing, cooling condition*

1. Introduction

Copper alloys are widely used in electronic connectors and semiconductor lead-frames. Recently, the demand for the miniaturization of such electronic components, along with high reliabilities, increased, particularly for use in mobile phones and other electronic devices. These trends are significant driving forces in the development of high-strength and electrical-conductivity copper alloys. Therefore, precipitation-hardening copper alloys have received considerable attention for use in these applications compared to solid-solution-hardening phosphor bronzes.

Among precipitation-hardening copper alloys, Corson alloys, which contain Ni and Si as the main alloying elements, are primarily used because of their excellent balances of strength, electrical conductivity, and bend formability [1–3]. Corson alloys with higher Ni and Si contents, in particular, exhibit higher strengths because of their high-volume fractions of the precipitate Ni_2Si [4]. These alloys contribute to the further miniaturization and higher reliabilities and degrees of design of connectors, lead frames, and other electronic devices [5]. Therefore, Corson alloys containing higher amounts of Ni and Si are indispensable materials in the forthcoming information society.

Hot cracking is a significant issue for copper alloys [6, 7], but most research regarding hot cracking has been conducted using steel and aluminum alloys. In such studies, several models have been proposed to assess susceptibility to hot cracking [8, 9]. The basic theory is that the temperature range where residual liquid healing does not occur is crucial in explaining hot cracking. As the capacity for liquid healing is strongly influenced by the dendritic shape, understanding the dendritic growth behavior during solidification is necessary in evaluating hot cracking susceptibility [9]. Nevertheless, very few studies regarding copper alloys have been reported in this field of research [10–14]. For example, Oya *et al.* focused on Cu-Sn and Cu-Zn alloys to investigate the effects of the microstructures and additive elements on the hot cracking susceptibilities of the alloys. However, quantitative evaluation is insufficient in predicting hot cracking, and furthermore, no study on Corson alloys have been reported. Therefore, quantitatively evaluating hot cracking susceptibilities of Corson alloys is critical.

Recently, numerous studies have been conducted regarding the *in-situ* observation of the solidified microstructure [15, 16]. For example, Yasuda *et al.* reported the *in-situ* observation of Fe-C alloys during solidification using synchrotron X-rays radiation at SPring-8 [16]. Although these *in-situ* observation methods are extremely useful, they are not viable for conducting laboratory-scale experiments, and they are also inadequate for large-scale casting experiments. Considering the experimental limitation, a quantitative, low-cost investigation of the effects of the solidification conditions on the dendritic growth behavior can only be performed by predicting the solidified microstructure using simulation methods. Previously, we experimentally investigated the solidified microstructures of Corson alloys and analyzed the primary and secondary dendrite arm spacings (P- and S-DASs, respectively) after the completion of solidification [17]. In this study, the experimental data reported in our previous study are used to theoretically predict the P- and S-DASs of Corson alloys.

The numerical analysis of solidification microstructures began in the 1990s. Kobayashi conducted the first phase-field (PF) simulation to calculate dendrite growth during solidification by introducing a parameter, denoted the PF, that indicated the phase state [18]. The PF method is suitable

*[1]Graduate student, Osaka University
*[2]Corresponding author, E-mail: muto.yuki.wv9@jx-nmm.com

for predicting dendrite growth because introducing the PF parameter eliminates the necessity of following the interface and easily represents complex microstructural changes.

Owing to these advantages, numerous studies and systematizations using the PF method have been conducted on microstructure formation during the solidification of various materials [19–32]. For example, the S-DASs of aluminum and ferrous alloys were evaluated via 2D PF simulations, and the relationships between the S-DASs and cooling rate were analyzed [19–21]. Thereafter, the increase in computing power and development of efficient calculation methods enabled the calculation of the large-scale 3D dendrite growth of Al-Si alloy [22]. These 3D PF calculations were also applied to other alloys, such as Al-Cu and Fe-Mn alloys, which enabled more detailed evaluations of their microstructures during solidification [23–25]. Recently, an inverse analysis method was proposed to determine the anisotropies of solid-liquid interface energies by combining PF simulations and machine learning [26, 27], where the estimated anisotropy of an Fe-Mn alloy was 0.021 [27].

However, there are few research reports on the application of the PF method to the solidification microstructures of copper alloys. The only report on copper-based alloys [33] is limited to Cu-Sn alloys, which are conventional solid-solution-strengthened copper alloys. In this study, the influence of the solidification rate on the partition coefficient was assessed, but crucial microstructural characteristics such as P-DAS and S-DAS, were not analyzed. Furthermore, PF parameters related to the anisotropy of interface energy were not provided.

We have conducted the first experimental observations of the solidification microstructures to predict hot cracking susceptibility using precipitation-strengthened copper alloys (Corson alloys) [17]. The present study aims to replicate these experimentally observed microstructures using the PF method to demonstrate whether it can be utilized for alloys under the actual manufacturing solidification conditions of practical copper alloys for the first time. By comparing P-DAS and S-DAS from both experiments and PF computations, we estimate the calculation parameters for the interface energy and reproduce the effect of cooling rate on the solidification microstructures of Corson alloys. Finally, we will evaluate whether the obtained parameters and simulated microstructures can be utilized in future research to predict hot cracking in precipitation-hardened copper alloys.

2. Phase-Field Method

In the PF method [28, 32, 34, 35], the phase-field, ϕ is introduced to represent the phase state. When calculating the solidification microstructure of a single solid phase, for example, the phase-field is set $\phi = 0$ for the solid phase, $\phi = 1$ for the liquid phase and, $0 < \phi < 1$ for the solid/liquid interface, respectively. The solid/liquid interface in the PF model has a finite width, allowing the PF to continuously change, which enables numerical differentiation.

The PF equation is derived to minimize the free energy of the system ($F(\phi)$), which is set by integrating the free energy density (f), as shown in eq. (1). The free energy density for solidification is composed of the chemical free energy density (f_{chem}) and interface free energy density (f_{intf}), as shown in eq. (2).

$$F(\phi) = \int f(\phi) dV \tag{1}$$

$$f = f_{chem} + f_{intf} \tag{2}$$

where

$$f_{chem} = \phi f_l + (1-\phi) f_s,$$

$$f_{intf} = \frac{4\sigma}{\eta}\left\{\frac{\eta^2}{\pi^2}(\nabla\phi)^2 + \phi(1-\phi)\right\}.$$

f_l and f_s are the free energy of liquid and solid phases, η is the interface width and σ is the solid/liquid interface energy. As the PF variable is a non-conservative quantity, the PF equation with an anisotropic interface energy is expressed as [28, 32],

$$\begin{aligned}\frac{\partial\phi}{\partial t} &= -M\frac{\delta F}{\delta\phi} \\ &= M\left\{(\sigma+\sigma'')\left[\nabla^2\phi - \frac{\pi^2}{2\eta^2}(1-2\phi)\right]\right. \\ &\quad \left. - \frac{\pi}{\eta}\sqrt{\phi(1-\phi)}(f_l - f_s)\right\}\end{aligned} \tag{3}$$

$$\sigma = \bar{\sigma}(1 - \sigma_4 \cos 4\theta) \tag{4}$$

where σ'' is the second derivative of the interface energy with respect to θ. M is the interface mobility and related to the interface kinetic coefficient μ as follows,

$$\frac{M}{1 - M\frac{\eta}{8}\Delta S m_l^i [D_l^{ij}]^{-1}(c_s^j - c_l^j)} = \mu \tag{5}$$

When the solidification condition can be considered a diffusion-controlled reaction, in other words, when the interface kinetic coefficient is effectively infinite, the mobility is expressed as,

$$M^{-1} = \frac{\eta}{8}\Delta S m_l^i [D_l^{ij}]^{-1}(c_s^j - c_l^j) \tag{6}$$

where ΔS is the entropy at the interface temperature, m_l^i is the liquidus slope ($m_l^i < 0$), D_l^{ij} is the interdiffusion coefficient of the liquid, and c_s^j and c_l^j are the composition of each component in the solid and liquid phases, respectively. Note that if μ is sufficiently large, the calculation results do not depend on M because the interface motion is controlled by solute-diffusion.

As the interface motion depends on the concentration and temperature fields, the PF equation is coupled with the concentration and/or temperature field equations. The time evolution equation for concentration can be expressed by the following diffusion equation incorporating the anti-trapping current commonly used in the PF method [35].

$$\frac{\partial c^{i*}}{\partial t} = \nabla\left[((1-\phi)d^i\nabla c_l^{i*}) + \alpha^{i*}\frac{\partial\phi}{\partial t}\frac{\nabla\phi}{|\nabla\phi|}\right] \tag{7}$$

$$\alpha^{i*} = \frac{\eta}{\pi}(c_l^{i*} - c_s^{i*})\sqrt{\phi(1-\phi)} \tag{8}$$

where d^i is diagonal matrix of the interdiffusion coefficient representing the diffusion matrix. d^i means eigenvalue of D_l^{ij} when D_l^{ij} is diagonalized by using transformation matrix P.

c^{i*} and α^{i*} represent by using P as $c^{i*} = Pc^i$ and $\alpha^{i*} = P\alpha^i$, where c^i and α^i are the composition and antitrapping current coefficient of component i. Because of high diffusivity of heat compared to solute, temperature field was simulated in one-dimensional calculation with lager mesh size than that of concentration by the following equation [36, 37]. The direction was set as parallel to the that of temperature gradient.

$$\frac{\partial T}{\partial t} = \frac{1}{\overline{C_p}} \left\{ \nabla(PF_l\lambda_l + PF_s\lambda_s)\nabla T + \left(H_l \frac{\partial PF_l}{\partial t} + H_s \frac{\partial PF_s}{\partial t} \right) \right\} \quad (9)$$

where $\overline{C_p}$ is the average heat capacity, PF_l, PF_s are the average fraction, λ_l, λ_s are the heat diffusivity, and H_l, H_s are the enthalpy of liquid and solid phase in each temperature grid cell.

The cooling rate of conventional casting process is sufficiently slow to satisfy a local-equilibrium condition. This condition requires the constraint of equal diffusion potentials for the phases within the interface to minimize the local Gibbs energy. In this study, the thermodynamic driving force, $f_s - f_l = \Delta G$, in the PF equation is calculated using the commercial thermodynamic database of Cu-based alloys to satisfy the equal diffusion potentials and their concentrations as follows [34],

$$\Delta G = \frac{1}{v_m}(\mu_s^0 - \mu_l^0) \quad (10)$$

where v_m is molar volume and μ_s^0, μ_l^0 are the diffusion potentials of the solid and liquid phases.

3. Casting Method with Various Cooling Rates Based on the Mizuta Method

To evaluate the effect of the cooling rate on the casting microstructure, Corson alloy ingots were prepared using a casting method denoted the Mizuta method [38]. The details of the experimental setup are described in a previous study [17].

In the Mizuta method, a copper alloy is melted in a crucible via induction heating. The crucible containing the copper alloy was air- or water-cooled. The ingots were unidirectionally solidified from the wall of the cylindrical crucible toward the center, the temperatures at several points parallel to the solidification direction were measured, and the microstructures were observed using an optical microscope at a location corresponding to the temperature measurement points. The casting microstructures and cooling curves were obtained under three types of water- and air-cooling conditions using various observation positions.

The compositions of the ingots were Cu-4.8 mass%Ni-1.1 mass%Si and Cu-4.7 mass%Ni-1.1 mass%Si for water and air cooling, respectively. Figure 1 shows the cooling curves obtained in this experiment, where the distance represents that from the crucible wall to the position of temperature measurement. The cooling rate decreased as the distance from the crucible wall increased. Figure 2 presents the microstructural observations under each cooling condition, where the white arrows indicate the direction toward the center of the crucible. The dendrites grew from the wall to the center of the crucible, and the cooling rate strongly influenced both the primary and secondary dendrite microstructures. In the final stage of casting, the secondary arms of air-cooled dendrites were coarsened. Based on these observations, the P- and S-DASs were evaluated, and they are summarized in Table 1.

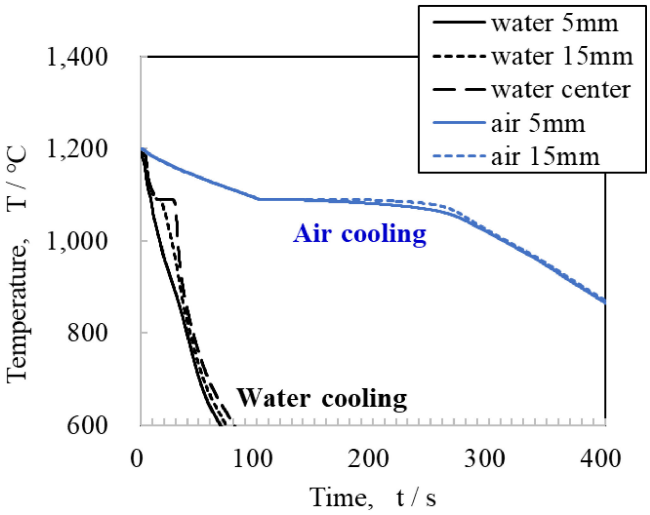

Fig. 1 Cooling curves obtained using the Mizuta method at each position from the crucible wall under water and air cooling [17].

4. Numerical Analysis of Microstructures during Casting by Phase-Field Method

4.1 Simulation condition

In this study, PF calculations were performed using the commercial software MICRESS (version 7.1) [34]. MICRESS employs the API provided by the thermodynamic calculation software Thermo-Calc (version 2022b) [39], which allowed users to access their thermodynamic and mobility databases. The present computations incorporate free energy data from TCCU5, TCS Cu-Based Alloys Database, and kinetic data from MOBCU5, TCS Cu-Based Alloys Mobility Database.

While 2D and 3D calculations are not identical, this study employed 2D calculations due to their lower computational costs. This is because we consider that 2D PF simulations provide reasonable results for evaluating the effects of the cooling condition on the S-DASs by comparing the simulated and experimental results. Several studies have shown that 2D calculations can accurately predict the experimental S-DAS [19, 20, 40]. Additionally, one of these studies [40] demonstrated that the S-DASs predicted via 3D and 2D PF calculations are almost the same. Consequently, as we considered that the deviation from the experimental values is not significant even when using 2D calculations, we utilized 2D PF simulations in this study.

Figure 3 illustrates the simulation conditions employed in reproducing the microstructures generated via unidirectional dendritic solidification, as obtained using the Mizuta method. The calculation domain was denoted by the x- and z-directions, as shown in Fig. 3.

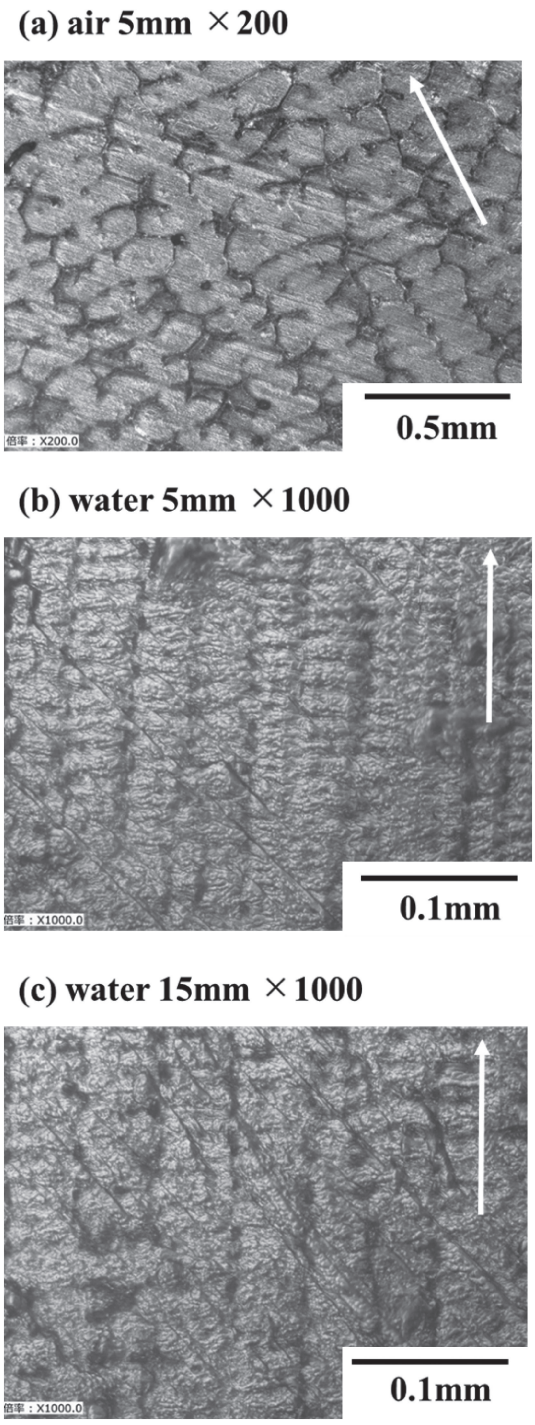

Fig. 2 Microstructural observations under an air-cooling condition of (a) 5 mm and water-cooling conditions of (b) 5 and (c) 15 mm. The white arrows indicate the solidification directions. Reprinted with permission from Ref. [17].

Table 1 Primary and secondary dendrite arm spacings [17]. The number in parentheses indicate the standard deviations.

Cooling condition	Measurement point	Primary dendrite arm spacing μm	Secondary dendrite arm spacing μm
air	5 mm	236 (51)	97 (10)
water	5 mm	32 (3)	12 (2)
	15 mm	40 (2)	18 (1)

Considering that a single columnar dendrite can represent the whole experimental microstructure, the size of the calculation domain was the P-DAS and approximately 20 times the S-DAS in the x- and z-directions, respectively. The initial temperature at the bottom of temperature domain was 0.5 K lower than the equilibrium liquid temperature. Temperature conditions were set to reproduce experimental results. In our previously paper on the experiment [17], we placed two thermocouples along the growth direction of columnar dendrites. The thermocouple temperature on the mold side was directly input for the temperature at the bottom of the calculation domain, and the temperature in the calculation domain is computed using the eq. (9), as shown in Section 2. Mesh size of temperature simulation was set as 100 μm. The thermophysical properties in the equation, enthalpy, H, and specific heat capacity, $\overline{C_p}$, are referenced from the thermodynamic database, TCCU5. The thermal conductivity, λ, was preliminary calculated to reproduce the measured temperature by the second thermocouple. The comparison between experimental and simulated cooling curves was shown in Fig. 4.

An initial nucleus, which was represented as a dendrite tip that had grown to the point of temperature measurement, was placed at the center of the bottom of the calculation domain. The angle between the preferred growth direction of the initial solid and the direction of the temperature gradient was set to 0°, and the boundary conditions were set as periodic and adiabatic in the x- and z-directions, respectively. This calculation was focused on single-dendrite growth within the experimentally observed microstructure.

The PF simulations were performed by moving the calculation domain in the z-direction following the dendrite tip. In the initial stage of the calculation, the calculation domain was fixed until the dendrite tip approached the top of the domain. The calculation domain was then moved such that the distance between the dendrite tip and top of the domain was maintained at 50 or 385 μm under water- or air-cooling, respectively. The computational domain was moved until the tip velocity reached a steady state, and the stage at which the tip velocity stabilized and the stage prior were denoted the steady and unsteady state, respectively. After entering the steady state, the calculation domain was fixed, and dendrite coarsening process was calculated. This calculation setup was used to avoid an unsteady state in the early stages of the calculation to compare the experimental and calculated microstructures.

The physical properties and simulation parameters used in the calculations are shown in Table 2 and Table 3, respectively. To reduce the computational cost, the driving force was calculated by linearizing the phase diagram obtained using the TCCU5 with the average concentration in each phase. The linearization routine was applied at intervals of 0.1 and 1.0 s under water and air cooling, respectively. Three meshes were set at each interface, and the appropriate time step was automatically calculated by the software. The interface properties, such as the solid-liquid interface energy and its anisotropy, are not well-defined and vary depending on the alloy system. In this study, these properties of the Corson alloy were estimated to reproduce the experimental microstructure through pre-calculations

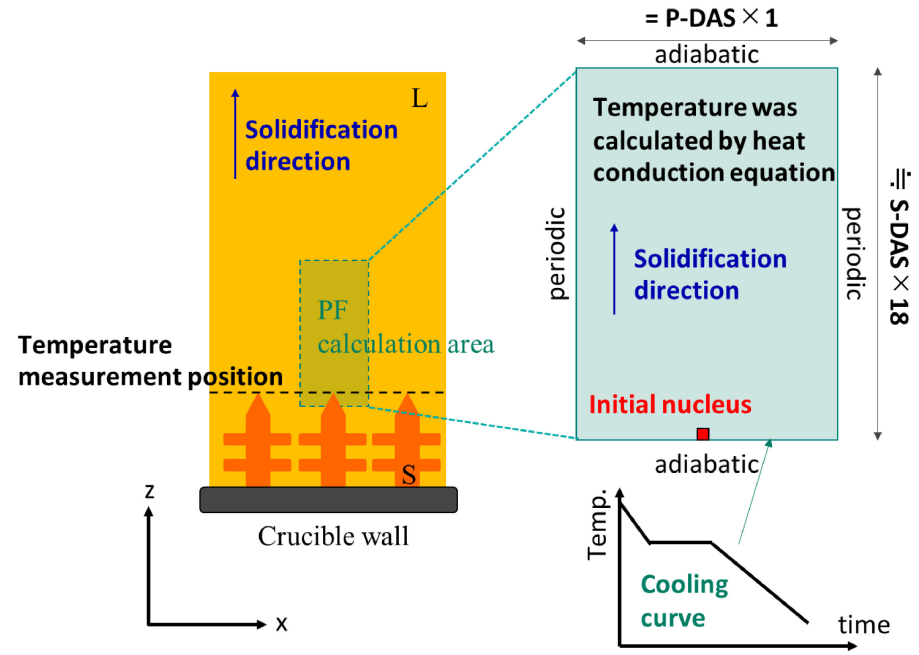

Fig. 3 Pattern diagram of the phase-field (PF) simulation condition.

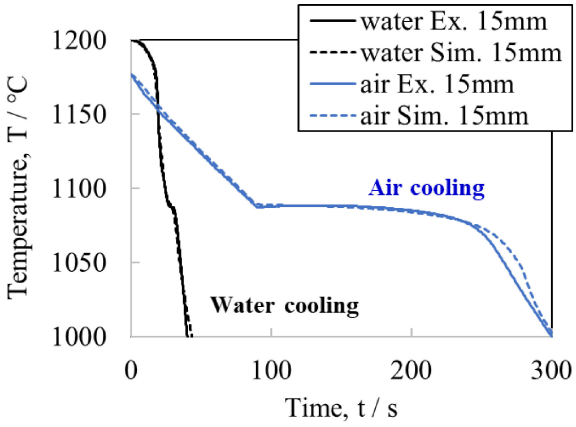

Fig. 4 Comparison between experimental and simulated cooling curves at 15 mm away from the crucible wall under water and air cooling.

Table 2 Physical properties used in the phase-field simulations.

Physical property	Interface energy	Interface kinetic coefficient	Anisotropy of interface energy
Symbol	$\bar{\sigma}$	μ	σ_4
Unit	$\times 10^{-5}$ J/cm^2	cm^4/Js	-
Value	1.0, 1.77, 3.0	10	0.010, 0.013, 0.017, 0.027

Table 3 Phase-field simulation parameters.

Calculation parameter	Cooling rate	Mesh size	Time step of the phase-diagram update
Symbol	CR	dx	-
Unit	K/s	μm	s
Value	11.7 (Water, 5mm) 6.6 (Water, 15mm)	0.125	0.1
	0.4 (Air, 5mm)	0.5	1

under water cooling. The chemical composition used in pre-calculations was set as Cu-4.5 mass%Ni-1.07 mass%Si (the target composition in the experiment), and the interface energy and its anisotropy were varied within the ranges of 1.0×10^{-5} to 3.0×10^{-5} J/cm^2 and 0.010 to 0.027, respectively. The ranges for the estimation were determined based on existing research, and the respective experimental and calculated interface energy of pure copper were 1.77×10^{-5} J/cm^2 [41] and 1.957×10^{-5} J/cm^2 [42]. The anisotropy of the interface energy estimated via or used in the PF simulations ranges from 0.005 to 0.05 [25, 27, 42–48]. These estimated interface properties were adopted in the subsequently performed calculations, and a large interface kinetic coefficient was used to calculate the interface mobility by eq. (6). The anisotropy of the interface mobility was not introduced.

4.2 Simulation results

The properties of the solid-liquid interface considerably influence the formation of solidification microstructures. A higher interface energy generally inhibits secondary arm formation, resulting in columnar structures. Meanwhile, an interface energy with a sufficiently large anisotropy is indispensable in generating well-defined dendritic microstructures. Figure 5 shows a representative calculation example from preliminary calculations. The effect of the interface energy on the microstructure of the Corson alloy was evaluated. These calculations indicated that secondary dendrite arms were well developed at an interface energy of 1.0×10^{-5} J/cm^2, whereas they were hardly generated at 3.0×10^{-5} J/cm^2. Varying the interface energy and its anisotropy within the above ranges reveals that respective values of 1.0×10^{-5} J/cm^2 and 0.013 could reproduce the experimentally observed S-DAS. Comparing these interface properties to those from other studies, the interface energy in this study was lower than the experimental value of pure

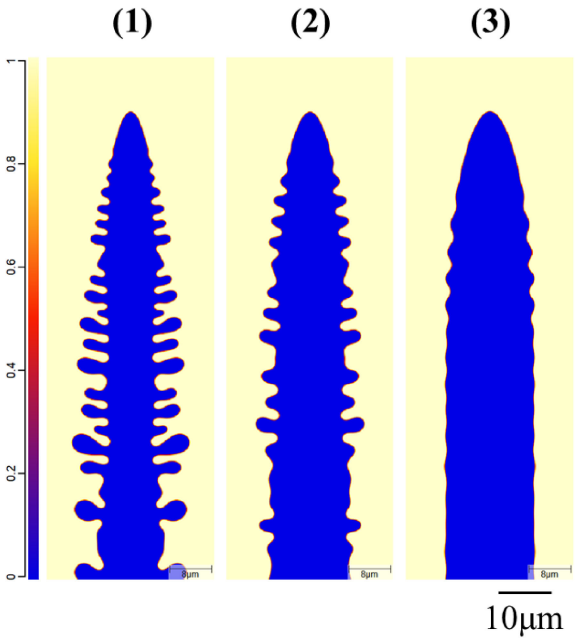

Fig. 5 Effects of interface energy on the pre-calculations at interface energies of (1) 1.0×10^{-5}, (2) 1.77×10^{-5}, and (3) 3.0×10^{-5} J/cm^2, with an anisotropy of 0.013.

copper of 1.77×10^{-5} J/cm^2 [41] and its anisotropy was lower than those (0.02–0.03) used in other PF simulations of ferrous alloys [25, 27, 48]. The determined interface properties were utilized in subsequent PF simulations.

Figure 6 shows the dendrite tip temperatures and solidification rate, as calculated via the PF simulations. In the initial stage of the calculation, dendrite growth was very slow, and the dendrite tip temperature decreased. The solidification rate then increased rapidly, the dendrite tip temperature reached a minimum, and the undercooling from the steady temperature was approximately 1 K. In the steady stage, the solidification rate remained constant, as shown in Fig. 6(b), or it exhibited a constant slope, as shown in Fig. 6(a) and (c). The changes in the calculated dendrite microstructures over time under water cooling (5 mm) are shown in Fig. 7. The figure panels show the microstructures at 0.7, 0.9, and 5.0 s after initiating the calculations. In the unsteady state, the secondary dendritic branches only began to develop in the middle of the dendrite, as shown in Fig. 7(1). When the dendrite tip temperature was approximately 1 K lower than that of the steady state, the secondary dendritic branches were well-developed, as shown in Fig. 7(2). The experimental results shown in Fig. 2 were considered for stable dendrite growth. Therefore, the calculated microstructure for comparison with the experimental results was selected from the steady stage, as shown in Fig. 7(3).

Under water cooling at 5 and 15 mm and air cooling at 5 mm, the steady states began after 5, 8, and 110 s, respectively. The longer the distance of dendrite growth was, the more likely the tip temperature is to deviate from the experimentally measured value. Therefore, to accurately evaluate the S-DAS using this simulation, coarsening process was calculated by fixing the calculation domain at the time of the initiation of the steady state.

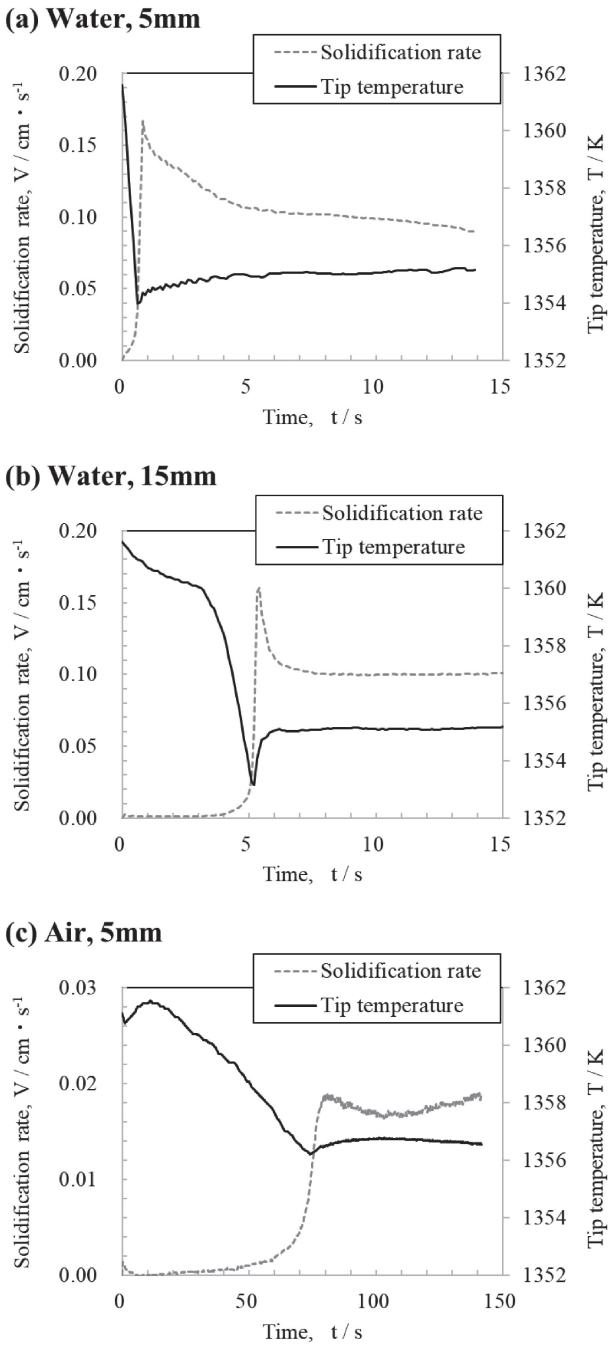

Fig. 6 Solidification rates and the dendrite tip temperature in the PF simulations under water-cooling conditions at (a) 5 and (b) 15 mm and an air-cooling condition at (c) 5 mm.

Figure 8 shows the results after coarsening process under water or air cooling at 5 mm. The solid fraction shown in Fig. 8(2) and (3) were 0.7 and 0.8, respectively. The results of PF simulation indicated that the primary dendrite trunks were thinner, and the secondary dendrites increased in length under air cooling compared to those of the respective primary and secondary dendrites under water cooling. This was consistent with the experimental results shown in Fig. 2, and this result suggested that this simulation could reproduce the effects of the cooling conditions on the shape of the dendrites. As dendrite coarsening process progressed, the trunks of the primary and secondary dendrites thicken.

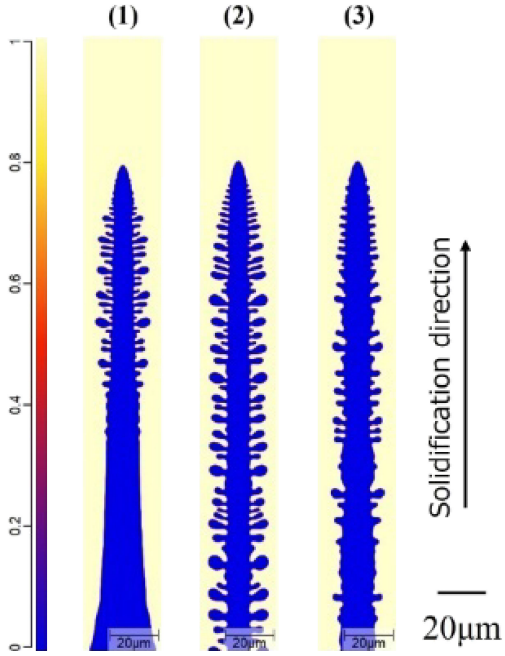

Fig. 7 Result of PF simulations of the dendrite structures at (1) 0.7, (2) 0.9, and (3) 5.0 s under water-cooling condition at 5 mm.

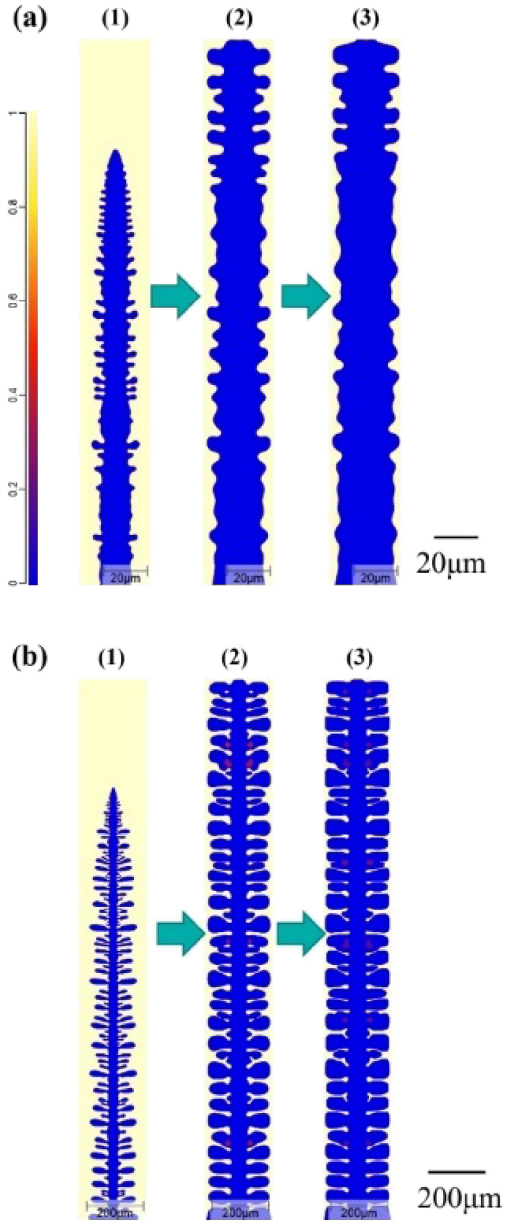

Fig. 8 Results of the PF simulations of the dendrite structures at various solidification rates: (a) water- and (b) air-cooling at 5 mm: (1) the initial structure used in simulating the coarsening process, and the structures at solid fraction (fs) = (2) 0.7 and (3) 0.8.

The S-DAS was evaluated using the results calculated at a solid fraction of 0.8 and compared with the experimental value. The calculated S-DAS was evaluated based on the distribution of the Ni concentration. The Ni concentration on a line parallel to the z-direction at a solid fraction of 0.8 under air cooling at 5 mm is shown in Fig. 9. The method of evaluating S-DAS was based on the measurement procedures of the Japan Institute of Light Metals [49]. The points at which the Ni concentration decreased to less than 5 wt% were identified as the solidification phases, and the S-DAS was determined by dividing the length of the line (Fig. 9) by the number of secondary dendritic branches. The S-DAS was evaluated in an area far from the top of the calculated domain to avoid the boundary effects at the top of the domain.

Figure 10 compares the experimentally obtained and PF-simulated S-DASs. The horizontal axis represents the cooling rate because the experimental S-DAS can be expressed as a multiplier approximation of the cooling rate [17]. The S-DASs obtained via the PF simulations are consistent with the experimentally obtained values.

Based on these results, it was concluded that the microstructure formed during the casting of a Corson alloy could be accurately predicted using the PF method by considering various parameters.

5. Conclusions

Calculations were performed to reproduce the microstructure of a Corson alloy during casting using the PF method. The microstructures were obtained from unidirectionally solidified ingots produced using the Mizuta method under several cooling conditions. The results are summarized as follows,

(1) The PF simulation was conducted using the commercial MICRESS software (version 7.1). The calculation domain was moved with the dendrite tip until the steady state was reached, and coarsening process was calculated to yield microstructures that could be compared to the experimental observations.

(2) Comparing the simulated results obtained under air or water cooling confirmed that the primary dendrite trunks were thinner and the secondary dendrites were longer and well-developed under air cooling, which successfully reproduced the experimental results.

(3) The S-DAS determined via PF simulation was evaluated using the Ni concentration profile, and the results were consistent with the experimental observations.

(4) The interface properties used in the PF simulations of the Corson alloy were compared to those reported in other studies, and the interface energy used in this study was lower than the experimental value of pure copper,

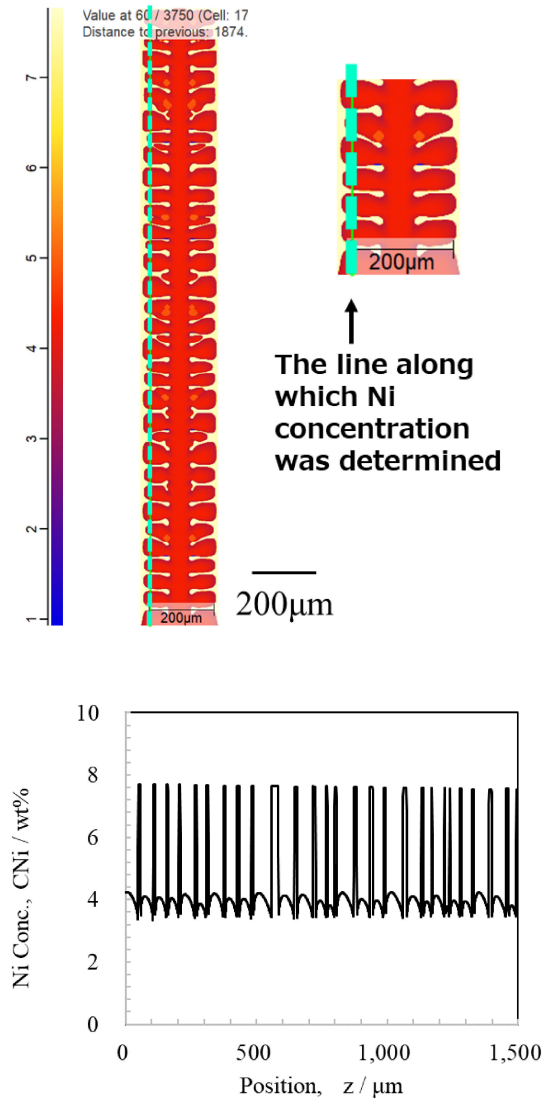

Fig. 9 Ni concentration profile along a longitudinal line under air-cooling condition at 5 mm and fs = 0.8.

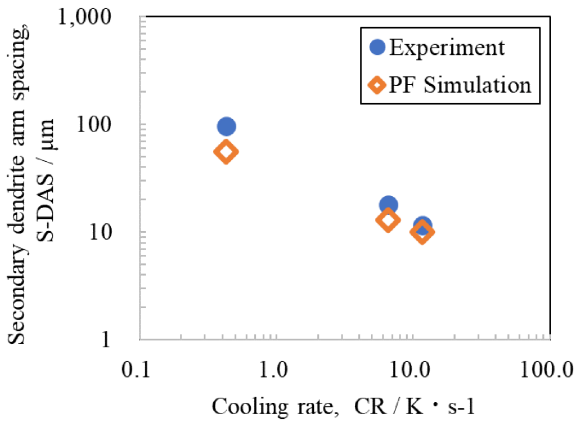

Fig. 10 Secondary dendrite arm spacings determined via PF simulation and the experimental results.

and its anisotropy was lower than those used in other PF simulations of ferrous alloys.

The capacity of this simulation method to predict the dendrite microstructure using its temperature history during solidification was critical in predicting the hot cracking susceptibility. However, to predict the hot cracking susceptibility during casting, it is insufficient only to correctly simulate solidified microstructure. Thus, further investigations of the hot-cracking susceptibility shall be conducted using simulation methods.

Acknowledgments

I would like to thank M. Segawa at the ITOCHU Techno-Solutions Corporation for their useful instructions and assistance with the PF simulations using the MICRESS version 7.1 software.

REFERENCES

[1] M.G. Corson: Copper Alloy Systems with Variable Alpha Range and Their Use in the Hardening of Copper, Proc. Inst. Metals Div., AIME, (1927) pp. 435–450.
[2] S.A. Lockyer and F.W. Noble: Precipitate structure in a Cu-Ni-Si alloy, J. Mater. Sci. **29** (1994) 218–226.
[3] C. Watanabe, H. Hiraide, Z. Zhang and R. Monzen: Microstructure and mechanical properties of Cu-Ni-Si alloys, J. Soc. Mater. Sci. Jpn. **54** (2005) 717–723.
[4] K. Hirose: Development of Grain Refinement Technique Using Cr Addition in Cu-Ni-Si Alloys, The Furukawa Electric Review, **21** (2008) 23–27.
[5] JX Metals Corporation: https://www.jx-nmm.com/english/products/alloy/copper/03cunisi/, (cited 2024-06-18).
[6] R. Takai and M. Yoshida: Hot tearing susceptibility of non-ferrous alloys (part 1), J. JFS **87** (2015) 569–575.
[7] R. Takai and M. Yoshida: Solidification cracking susceptibility of non-ferrous alloys (part 2), J. JFS **87** (2015) 576–581.
[8] A. Zama and M. Yoshida: Review on the theories and criteria of solidification cracking of aluminum alloys (after 1990), J. JFS **82** (2010) 640–646.
[9] R. Takai, M. Otaki and M. Yoshida: Hot tearing susceptibility of aluminum and magnesium alloys during casting (Part 2), J. JILM **68** (2018) 79–90.
[10] S. Oya, Y. Yamane, M. Sayashi and S. Shinozuka: Hot tearing in Cu-Sn alloys in relation to the freezing range and solidification structure, J. JFS **51** (1979) 485–489.
[11] S. Oya, Z. Toda and Y. Ōya: Hot tearing in Cu-Zn and Cu-Al binary alloys, J. JFS **51** (1979) 533–538.
[12] S. Oya and Z. Toda: Grain refining and hot tearing in brass castings, J. JFS **51** (1979) 596–601.
[13] S. Oya and Z. Toda: Dendrite morphology and hot tearing in brass castings, J. JFS **51** (1979) 709–714.
[14] S. Oya and Z. Toda: Low melting point inclusions and hot tearing in brass castings, J. JFS **52** (1980) 22–27.
[15] B. Cai, J. Wang, A. Kao, K. Pericleous, A.B. Phillion, R.C. Atwood and P.D. Lee: 4D synchrotron X-ray tomographic quantification of the transition from cellular to dendrite growth during directional solidification, Acta Mater. **117** (2016) 160–169.
[16] H. Yasuda, K. Morishita, N. Nakatsuka, T. Nishimura, M. Yoshiya, A. Sugiyama, K. Uesugi and A. Takeuchi: Dendrite fragmentation induced by massive-like δ–γ transformation in Fe–C alloys, Nat. Commun. **10** (2019) 3183.
[17] Y. Muto, K. Kammuri, J. Miyake, T. Kurashiki and H. Mori: Effect of cooling condition on microstructure after unidirectional solidification of Cu-Ni-Si alloys, J. Jpn. Inst. Met. Mater. **87** (2023) 200–204.
[18] R. Kobayashi: Modeling and numerical simulations of dendritic crystal growth, Phys. D **63** (1993) 410–423.
[19] M. Ode, S.G. Kim, W.T. Kim and T. Suzuki: Numerical Prediction of the Secondary Dendrite Arm Spacing Using a Phase-field Model, ISIJ Int. **41** (2001) 345–349.
[20] Y. Natsume and H. Ishida: Characterization of Dendrite Morphology for Al-Based Alloy by Phase-field Model, Proc. 12th Int. Conf. on Aluminium Alloys, (2010) pp. 1746–1751.

[21] A. Roósz, A. Rónaföldi, M. Svéda and Z. Veres: Comparison of Dynamical and Empirical Simulation Methods of Secondary Dendrite Arm Coarsening, Crystals **12** (2022) 1834–1852.
[22] T. Shimokawabe, T. Aoki, T. Takaki and T. Endo: Peta-scale phase-field simulation for dendritic solidification on the TSUBAME 2.0 supercomputer, Proc. 2011 Int. Conf. for High Performance Computing, Networking, Storage and Analysis, (2011) pp. 1–11.
[23] T. Takaki: Phase-field Modeling and Simulations of Dendrite Growth, ISIJ Int. **54** (2014) 437–444.
[24] B. Bellón, A.K. Boukellal, T. Isensee, O.M. Wellborn, K.P. Trumble, M.J.M. Krane, M.S. Titus, D. Tourret and J. LLorca: Multiscale prediction of microstructure length scales in metallic alloy casting, Acta Mater. **207** (2021) 116686.
[25] M. Ohno: Quantitative Phase-field Modeling and Simulations of Solidification Microstructures, ISIJ Int. **60** (2020) 2745–2754.
[26] G. Kim, R. Yamada, T. Takaki, Y. Shibuta and M. Ohno: Inverse analysis of anisotropy of solid-liquid interfacial free energy based on machine learning, Comput. Mater. Sci. **207** (2022) 111294.
[27] S. Fukuzawa, R. Yamada and M. Ohno: Development of machine learning model for inverse analysis of anisotropy strength of interfacial energy from microsegregation, Collected Abstracts of the 2022 Autumn Meeting of the Japan Inst. Metals and Materials, (2022) No. 110.
[28] I. Steinbach: Phase-field models in materials science, Model. Simul. Mater. Sci. Eng. **17** (2009) 073001.
[29] M. Asta, C. Beckermann, A. Karma, W. Kurz, R. Napolitano, M. Plapp, G. Purdy, M. Rappaz and R. Trivedi: Solidification microstructures and solid-state parallels: Recent developments, future directions, Acta Mater. **57** (2009) 941–971.
[30] W. Kurz, M. Rappaz and R. Trivedi: Progress in modelling solidification microstructures in metals and alloys. Part II: dendrites from 2001 to 2018, Int. Mater. Rev. **66** (2021) 30–76.
[31] K. Wang, S. Lv, H. Wu, G. Wu, S. Wang, J. Gao, J. Zhu, X. Yang and X. Mao: Recent research progress on the phase-field model of microstructural evolution during metal solidification, Int. J. Miner. Metall. Mater. **30** (2023) 2095–2111.
[32] I. Steinbach and H. Salama: *Lectures on Phase Field*, (Springer, Bochum, 2023).
[33] K.G. Paradela, W.J.L. Garção, L.A.S. Baptista, R.C. Sales, V.C. Oliveira and A.F. Ferreira: The Effect of the Cooling Rate on the Microstructure and Microsegregation: An Experimental and Numerical Investigation of Solidification in Hypoperitectic Cu – 20 wt.% Sn Alloy, Mater. Res. **23** (2020) e20200110.
[34] MICRESS software, www.micress.de, (cited 2024-06-18).
[35] A. Carré, B. Böttger and M. Apel: Implementation of an antitrapping current for a multicomponent multiphase-field ansatz, J. Crys. Growth **380** (2013) 5–13.
[36] B. Böttger, M. Apel, B. Santillana and D.G. Eskin: Relationship Between Solidification Microstructure and Hot Cracking Susceptibility for Continuous Casting of Low-Carbon and High-Strength Low-Alloyed Steels: A Phase-Field Study, Metall. Mater. Trans. A **44** (2013) 3765–3777.
[37] B. Böttger, J. Eiken and M. Apel: Phase-field simulation of microstructure formation in technical castings – A self-consistent homoenthalpic approach to the micro–macro problem, J. Comput. Phys. **228** (2009) 6784–6795.
[38] H. Taniguchi, K. Osamura, A. Kikuchi and T. Mizuta: Behavior of Ti-based Ternary Compounds in High Tin Bronze Used for Nb_3Sn Superconducting Wires, J. Cryog. Soc. Jpn. **50** (2015) 186–193.
[39] Thermo-Calc software, https://thermocalc.com, (cited 2024-06-18).
[40] M. Ohno, M. Yamashita and K. Matsuura: Importance of microstructural evolution on prediction accuracy of microsegregation in Al-Cu and Fe-Mn alloys, Int. J. Heat Mass Transfer **132** (2019) 1004–1017.
[41] D. Turnbull: Formation of Crystal Nuclei in Liquid Metals, J. Appl. Phys. **21** (1950) 1022–1028.
[42] J.J. Hoyt, M. Asta and A. Karma: Atomistic and continuum modeling of dendritic solidification, Mater. Sci. Eng. Rep. **41** (2003) 121–163.
[43] M.E. Glicksman and N.B. Singh: Effects of crystal-melt interfacial energy anisotropy on dendritic morphology and growth kinetics, J. Crys. Growth **98** (1989) 277–284.
[44] E.R. Rubinstein and M.E. Glicksman: Dendritic grown kinetics and structure I. Pivalic acid, J. Crys. Growth **112** (1991) 84–96.
[45] M. Muschol, D. Liu and H.Z. Cummins: Surface-tension-anisotropy measurements of succinonitrile and pivalic acid: Comparison with microscopic solvability theory, Phys. Rev. A **46** (1992) 1038–1050.
[46] A. Karma and W.J. Rappel: Quantitative phase-field modeling of dendritic growth in two and three dimensions, Phys. Rev. E **57** (1998) 4323–4349.
[47] R.E. Napolitano, S. Liu and R. Trivedi: Experimental Measurement of Anisotropy in Crystal-Melt Interfacial Energy, Int. Sci. **10** (2002) 217–232.
[48] T. Suzuki, M. Ode, S.G. Kim and W.T. Kim: Phase-field model of dendritic growth, J. Crys. Growth **237–239** (2002) 125–131.
[49] Japan Institute of Light Metals, Committee of casting and solidification: Measurement of dendrite arm spacing, J. JILM **38** (1988) 54–60.